Encyclopedia of Earthquake Engineering
DOI 10.1007/978-3-642-36197-5_295-1

Earthquake Mechanisms and Stress Field

Václav Vavryčuk*
Institute of Geophysics, Czech Academy of Sciences, Praha 4, Czech Republic

Synonyms

Dynamics and mechanics of faulting; Earthquake source observations; Focal mechanism; Rock failure; Shear faulting; Tectonic stress; Tensile faulting

Introduction

Earthquakes are processes associated with the sudden rupture of rocks along cracks, fractures or faults exposed to stress field in the Earth's crust and lithosphere. If stress reaches a critical value exceeding strength of faults or fractures in rock, accumulated energy of elastic deformation is partially spent for anelastic deformations in the focal zone and partially released and radiated in the form of seismic waves. Stress in the Earth's crust causing earthquakes can be of tectonic or non-tectonic origin (Ruff 2002; Zoback 2007; Zang and Stephansson 2010). The main source of non-tectonic stress within the Earth is gravitational loading. This stress is vertical with largest lateral variations near the Earth's surface being more homogeneous at depth. On the other hand, tectonic stress is mostly horizontal and originates in forces driving the plate motions (Heidbach et al. 2008). These forces typically cause "ridge push" processes where lithospheric plates are pushed to move away from spreading ridge or "slab pull" processes where two plates are in collision and one of them is subducting into the asthenosphere (Fowler 1990). The global plate tectonics successfully explained concentration of large earthquakes on margins of the plates characterized by the presence of low strength zones exposed to large stresses. On regional and local scales, stress in the Earth's crust is also affected by topography and its compensation at depth, sediment loading or presence of any heterogeneity caused by variations of density, rigidity and rock rheology, by fluid flow in rocks or by presence of faults, cracks and micro-cracks in rocks.

Properties of the stress field and of the associated fracture processes in the Earth's crust are closely related (Scholz 2002). The most common type of fracturing is shear faulting but under special stress conditions also tensile faulting can be observed (Julian et al. 1998; Vavryčuk 2011b; see entry "▶ Non-Double-Couple Earthquakes"). Type of faulting depends on the stress field but also on the orientation of activated fractures or faults with respect to the stress (Vavryčuk 2011a). In addition, the slip vector for shear faulting is close to or coincides with the direction of the maximum shear stress acting on the fault (Wallace 1951; Bott 1959). Therefore, type of faulting, orientation of activated faults and direction of slip along activated faults serve as an important source of information about the stress field and its spatial and lateral variations within the Earth's crust.

In this entry, the basic concept of stress is introduced and its relation to earthquake mechanisms is explained (for description of focal mechanisms, see entry "▶ Earthquake Mechanism Description and Inversion"). Mohr's circle diagram and simple failure criteria are described and used for defining the fault instability, principal faults and principal focal mechanisms. Methods of determining stress from observed earthquake mechanisms are reported and their robustness is exemplified on numerical tests. Finally, several applications of stress inversions from earthquake mechanisms are listed.

*Email: vv@ig.cas.cz

Encyclopedia of Earthquake Engineering
DOI 10.1007/978-3-642-36197-5_295-1

Mathematical Description of Stress

Definition of Stress

Stress describes forces acting on a unit surface in a body (see Fig. 1a). Since the acting force and the normal of the unit surface are vectors, the stress is a tensor described by nine components

$$\boldsymbol{\tau} = \begin{bmatrix} \tau_{11} & \tau_{12} & \tau_{13} \\ \tau_{21} & \tau_{22} & \tau_{23} \\ \tau_{31} & \tau_{32} & \tau_{33} \end{bmatrix}. \tag{1}$$

The force acting on surface S with normal **n** is called traction **T**, and it is expressed as

$$T_i = \tau_{ij} n_j \tag{2}$$

with its normal and shear components σ_n and τ

$$\sigma_n = T_i n_i = \tau_{ij} n_i n_j, \tag{3}$$

$$\tau N_i = T_i - \sigma_n n_i = \tau_{ij} n_j - \tau_{jk} n_j n_k n_i = \tau_{kj} n_j (\delta_{ik} - n_i n_k), \tag{4}$$

where **N** is the direction of shear component τ and lies in surface S. Since stress is defined as that part of forces in a body which causes its deformation but not rotation, the stress tensor must be symmetric

$$\tau_{ij} = \tau_{ji}, \tag{5}$$

being described by six independent components only.

Mohr's Circle Diagram

The values of the stress tensor components depend on the system of coordinates, in which the components are measured. The coordinate system can always be rotated in the way that the stress tensor diagonalizes:

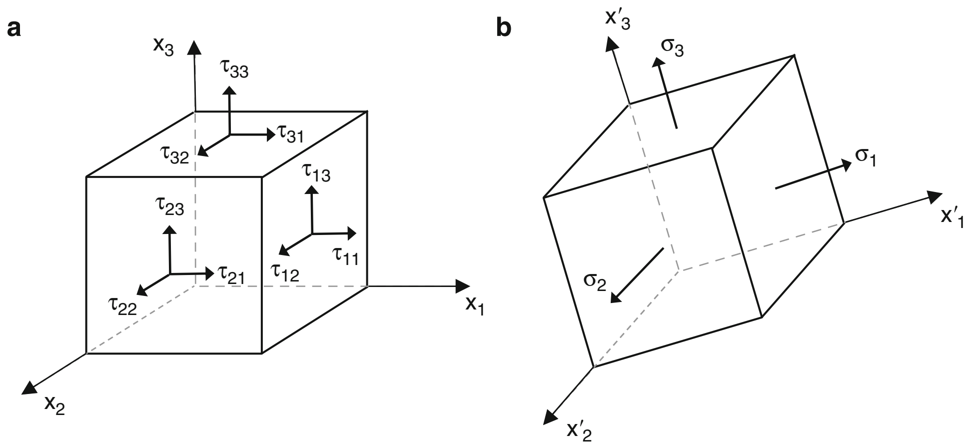

Fig. 1 Definition of the stress tensor in original Cartesian coordinate system (**a**) and in the rotated system of principal stress directions (**b**)

Encyclopedia of Earthquake Engineering
DOI 10.1007/978-3-642-36197-5_295-1

$$\boldsymbol{\tau} = \begin{bmatrix} \sigma_1 & 0 & 0 \\ 0 & \sigma_2 & 0 \\ 0 & 0 & \sigma_3 \end{bmatrix}, \tag{6}$$

where σ_1, σ_2 and σ_3 are called the maximum, intermediate and minimum principal stresses (compression is positive):

$$\sigma_1 \geq \sigma_2 \geq \sigma_3, \tag{7}$$

and the vectors defining this special coordinate system are called the principal stress directions or principal stress axes (see Fig. 1b). Mathematically, the principal stresses and their directions are found by calculating the eigenvalues and eigenvectors of the stress tensor.

The normal and shear components σ_n and τ of traction **T** (also called the normal and shear stresses) read in the system of principal stress directions

$$\sigma_n = \sigma_1 n_1^2 + \sigma_2 n_2^2 + \sigma_3 n_3^2, \tag{8}$$

$$\tau^2 = \sigma_1^2 n_1^2 + \sigma_2^2 n_2^2 + \sigma_3^2 n_3^2 - \sigma_n^2. \tag{9}$$

If principal stresses σ_1, σ_2 and σ_3 are fixed, then normal and shear stresses σ_n and τ are just functions of normal **n** of a fault and can be plotted in the Mohr's circle diagram (see Fig. 2). All permissible values of σ_n and τ must lie in the shaded area of the diagram (Jaeger et al. 2007; Mavko et al. 2009). If the sign of shear stress τ is important in the stress analysis, the Mohr's diagram is not plotted using semi-circles but full circles, see below.

When stress conditions in real rocks in the Earth's crust are studied, the Mohr's diagram is modified. Rocks are typically porous and contain pressurized fluids which influence overall stress in the rock (Scholz 2002). For example, fluids present inside a fault reduce the normal stress along the fault. If the fluid pressure is sufficiently high, fluids can even cause opening of the fault (see Fig. 3a). For this reason, effective normal stress σ is introduced as a difference between normal stress σ_n and pore-fluid pressure p

$$\sigma = \sigma_n - p, \tag{10}$$

and the Mohr's circle diagram is plotted in the σ–τ plane. Variation of pore-fluid pressure in the rock is projected into shifting of the Mohr's diagram along the σ-axis. The pore-fluid pressure acts against the

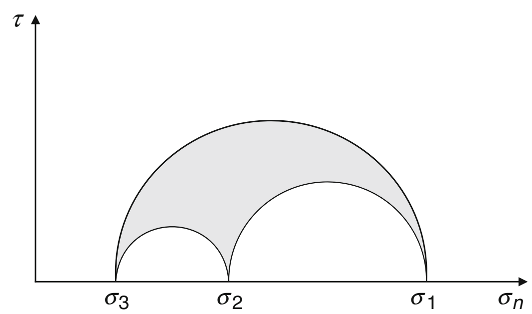

Fig. 2 Mohr's circle diagram. Quantities σ_n and τ are the normal and shear stresses along a fault, σ_1, σ_2 and σ_3 are the principal stresses. All permissible values of σ_n and τ acting on a fault must lie in the shaded area of the diagram

DOI 10.1007/978-3-642-36197-5_295-1

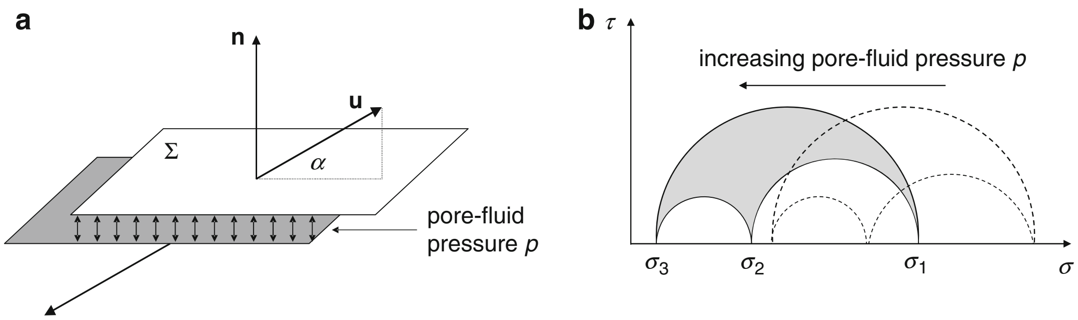

Fig. 3 Role of pore-fluid pressure in the rock. (**a**) Opening of the fault caused by fluids. (**b**) Shift of Mohr's circles due to increase of pore-fluid pressure. Σ is the fault, **u** is the slip vector and α is the deviation between the slip vector and the fault (the so-called slope angle, see Vavryčuk 2011b)

compressive normal stress and Mohr's circles are moved to the left with increasing pore-fluid pressure (see Fig. 3b).

Tectonic Stress and Faulting Regimes

Principal stress directions in the Earth's crust are frequently close to vertical and horizontal directions. This lead Anderson (1951) to developing a simple scheme connecting the basic stress regimes in the Earth's crust with type of faulting on a pre-existing fault in the crust (see Fig. 4). Anderson (1951) distinguishes three possible combinations of magnitudes of principal stresses: the vertical stress is maximum, intermediate or minimum with respect to the horizontal stresses. If the vertical stress is maximum, the hanging wall is moving downwards with respect to the foot wall and the normal faulting is observed along a deeply steeping fault. If the vertical stress is minimum, the crust is in horizontal compression and the hanging wall is moving upwards with respect to the foot wall and reverse faulting is observed along a shallow dipping fault. Finally, if the vertical stress is intermediate, the foot and hanging walls are moving horizontally and the strike slip faulting is observed along a nearly vertical fault. Obviously, the Anderson's classification is simple and does not cover all observations but still it proved to be valid for many seismically active regions and helpful for rough assessment of stress regime (Simpson 1997; Hardebeck and Michael 2006; see entry "▶ Earthquake Mechanisms and Tectonics").

Rock Failure and Earthquakes

If a rock is critically stressed in the Earth's crust, the rock is fractured and this fracturing is associated with an earthquake. In principle, an earthquake can occur on a newly developed fracture or on a pre-existing fault in the Earth's crust which is re-activated. The condition under which fracturing or faulting occurs is described by the so-called failure criteria. The simplest and most known criteria are the Griffith failure criterion derived from energy conditions imposed on propagating cracks in a rock, and the Mohr-Coulomb failure criterion (also called the Coulomb failure criterion) based on the concept of friction between two sliding blocks simulating the case of faulting on a pre-existing fault. Both failure criteria predict critical values of shear stress as a function of normal stress which lead to failure

$$\tau_c = f(\sigma). \tag{11}$$

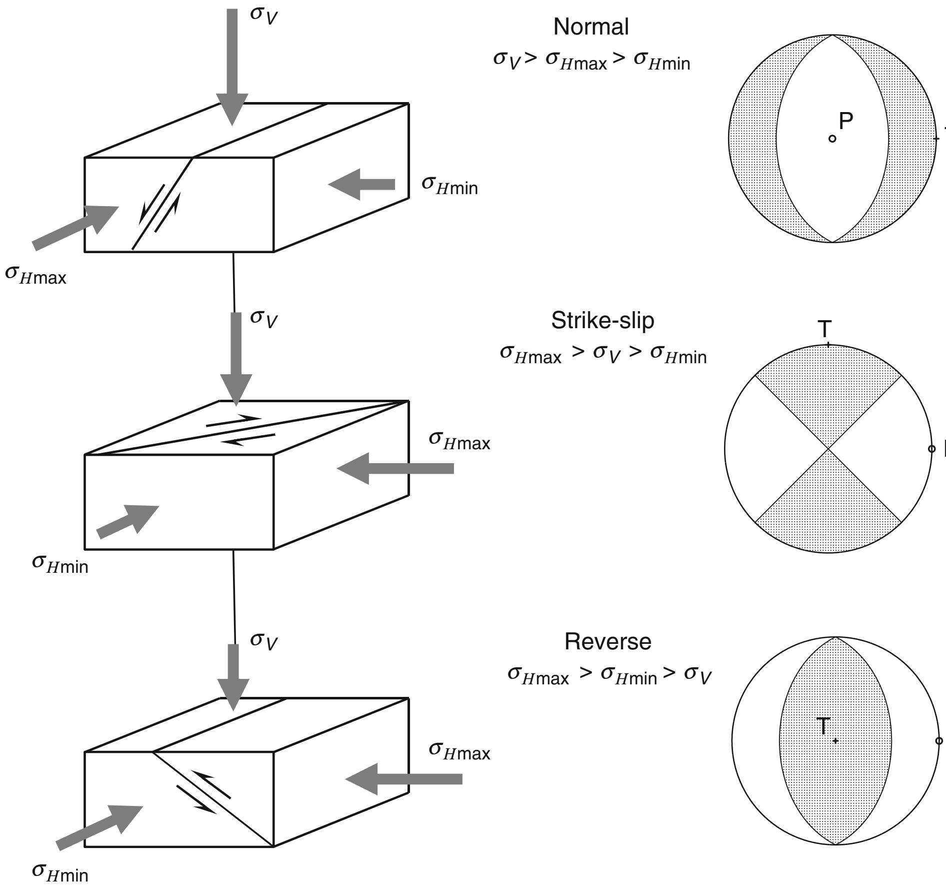

Fig. 4 Anderson's classification scheme of stress in the Earth's crust (*left*) and corresponding faulting regimes (*right*). The focal mechanisms with the P and T axes are shown in the lower-hemisphere equal-area projection

They can be plotted as the so called Mohr failure envelopes in the σ–τ diagram together with Mohr's circles and employed for analysis of stability of fractures or faults under given stress conditions. If the outer Mohr's circle touches the failure envelope, there is one fracture or fault which is unstable and can fail, its orientation being defined by inclination θ of the fault from the maximum stress direction (see Fig. 5a).

Griffith Failure Criterion

The Griffith theory of fracture predicts the failure envelope in the following form (Jaeger et al. 2007, Eq. 10.139):

$$\tau_c^2 = 4T_0(T_0 + \sigma), \tag{12}$$

where T_0 is the uniaxial tensile strength. The criterion is described by a parabola with the most curved part close to tensile normal stresses. The point at the parabola with the lowest value of normal stress (point 1 in Fig. 5b) corresponds to fracture lying along the maximum principal stress direction (maximum compression) σ_1 and opening during the fracture process. This physically describes the case of a pure tensile crack created, for example, by hydrofracturing due to fluid injection into the rock mass (Zoback 2007). The intersection of the parabola with the τ-axis (points 2 in Fig. 5b) defines the transition between tensile and shear modes of faulting and corresponds to fracture orientation which can be found using the following simple formula (Fischer and Guest 2011):

Encyclopedia of Earthquake Engineering
DOI 10.1007/978-3-642-36197-5_295-1

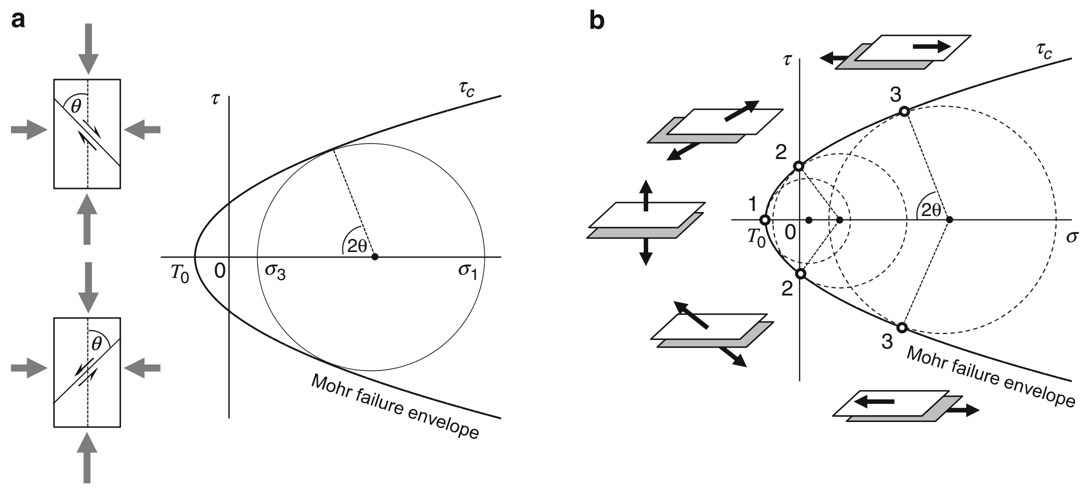

Fig. 5 Griffith failure criterion. (**a**) Scheme of a cylindrical specimen with a fracture created by loading with stresses $\sigma_1 > \sigma_2 = \sigma_3$ (*left*) and the corresponding Mohr's circle diagram (*right*). (**b**) Position of different faulting regimes on the Mohr failure envelope $\tau_c(\sigma)$. Point 1 – pure tensile faulting, points 2 – transition between tensile and pure shear faulting, points 3 – pure shear faulting. Angle θ defines the deviation of the fracture from the σ_1 direction, T_0 is the uniaxial tensile strength

$$\tan 2\theta_{\text{tensile}} = \left.\frac{\partial \tau_c}{\partial \sigma}\right|_{\sigma=0} = \left.\frac{\sqrt{T_0}}{\sqrt{T_0 + \sigma}}\right|_{\sigma=0} = 1, \tag{13}$$

and consequently $\theta_{\text{tensile}} = 22.5°$. Hence, tensile faulting (called also shear-tensile faulting) associated with fault opening can occur only for fractures which deviate from the direction of maximum compression with angle lower than θ_{tensile} (Mohr failure envelope between points 1 and 2 in Fig. 5b). For angles equal to or higher than θ_{tensile} only shear faulting mode can be observed (e.g., points 3 in Fig. 5b). As seen from Fig. 5b, the parabola is less curved for angles higher than θ_{tensile} and the Griffith failure criterion can be well approximated by the linear Mohr-Coulomb failure criterion, see below.

Mohr-Coulomb Failure Criterion

According to the Mohr-Coulomb failure criterion (Scholz 2002; Zoback 2007), shear stress on an activated fault must exceed critical value τ_c, which is calculated from cohesion C, fault friction μ and effective normal stress σ:

$$\tau_c = C + \mu\sigma, \tag{14}$$

or equivalently

$$\tau_c = C + \mu(\sigma_n - p), \tag{15}$$

where σ_n is the normal stress and p is the pore pressure. Friction μ for fractures was measured on rock samples in laboratory and ranges mostly between 0.6 and 0.8 (Byerlee 1978). The values of friction of faults in the Earth's crust are similar (Vavryčuk 2011a) but lower values like 0.2–0.4 have also been reported for some large-scale faults like the San Andreas fault (Scholz 2002).

If the Mohr-Coulomb failure criterion is satisfied (red area in Fig. 6), the fault becomes unstable and an earthquake occurs along this fault. The higher the shear stress difference, $\Delta\tau = \tau - \tau_c$, the higher the instability of the fault and the higher the susceptibility of the fault to be activated. A fault most susceptible

DOI 10.1007/978-3-642-36197-5_295-1

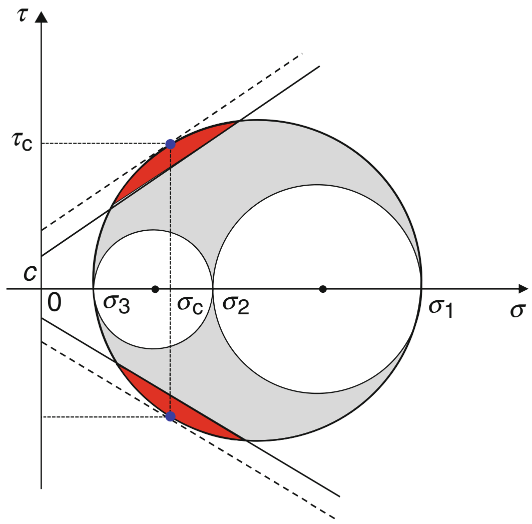

Fig. 6 Mohr-Coulomb failure criterion. The *red* area shows all possible orientations of fault planes which satisfy the Mohr-Coulomb failure criterion. The *blue dot* with shear and normal stresses τ_c and σ_c denotes the principal fault plane which is optimally oriented with respect to stress, and *C* denotes the cohesion

to failure is called the "principal" fault (Vavryčuk 2011a) being defined by the point in which the Mohr-Coulomb failure criterion touches the Mohr's circle diagram (blue point in Fig. 6)

A variety in possible orientations of unstable fault planes is demonstrated in Fig. 7. The left-hand plot of Fig. 7a shows the Mohr's diagram, the failure criterion and the positions of randomly distributed unstable fault planes satisfying the failure criterion. The middle and right-hand plots of Fig. 7a show the nodal lines and the P (pressure) and T (tension) axes for the corresponding focal mechanisms. The nodal lines and P/T axes inform about the predominant type of faulting and about the scatter in orientations of the unstable fault planes. Predominant faulting and its scatter are also projected into a scatter of the P/T axes, which form clusters of a specific shape and size (Fig. 7a, right-hand plot). The form of the clusters is best demonstrated using the projection of the Mohr-Coulomb failure criterion (Fig. 7b, blue line in the left-hand plot) onto the focal sphere (Fig. 7b, right-hand plot). The failure criterion curve splits into two closed curves for the P axes as well as for the T axes on the focal sphere corresponding to the failure conditions in the upper and lower half-planes in the Mohr's circle diagram. The two P/T failure curves may intersect each other or be separated. The area inside the failure curves define positions of the P/T axes of focal mechanisms conceivable under the given stress regime. The pattern when the P/T axes form two distinct sub-clusters is called as the "two-wing" or the "butterfly-wing" pattern (Vavryčuk 2011a). The butterfly wings are well separated provided that friction is high (0.5 or higher). If friction is low, the wings come closer or they overlap.

Fault Instability

Since differently oriented faults have a different susceptibility to be activated and thus being differently unstable in the given stress field, a quantity which measures this instability can be introduced. For example, the fault instability *I* of all fault orientations can be defined in the range from 0 to 1 (see Fig. 8) using the following formula (Vavryčuk et al. 2013):

$$I = \frac{\tau - \mu(\sigma - \sigma_1)}{\tau_c - \mu(\sigma_c - \sigma_1)}, \tag{16}$$

DOI 10.1007/978-3-642-36197-5_295-1

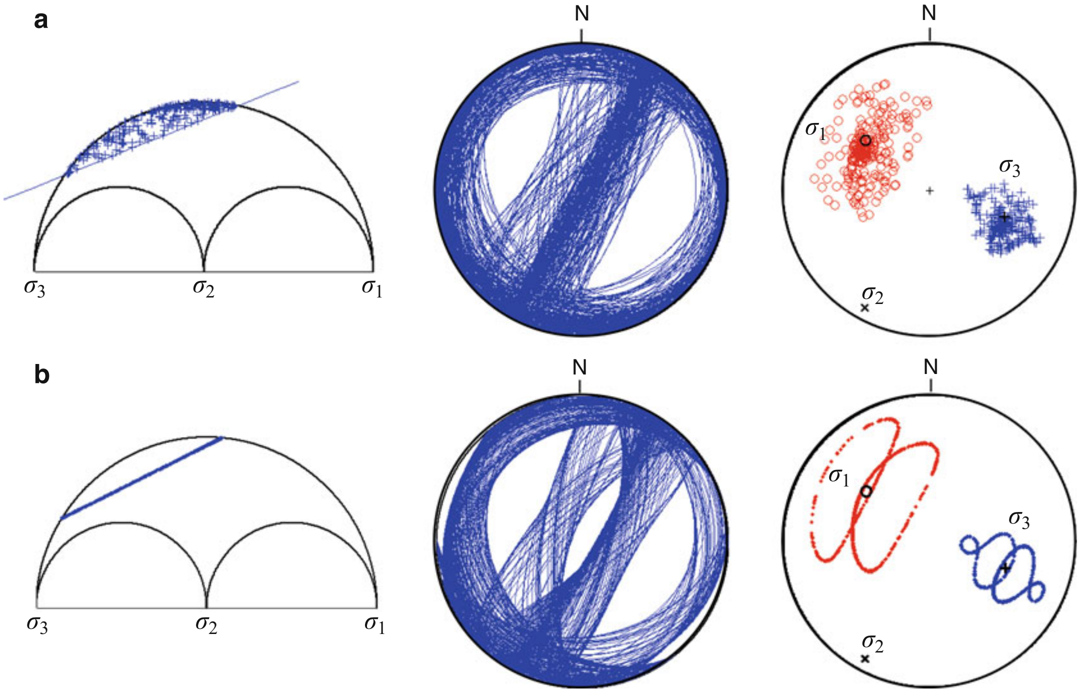

Fig. 7 Focal mechanisms associated with unstable fault planes. (**a**) Randomly distributed fault planes inside the unstable area of the Mohr's diagram (*left*), corresponding nodal lines (in the *middle*) and the P/T axes (*right*). The P (pressure) axes are marked by the *red circles*, the T (tension) axes by the *blue crosses*. (b) Fault planes corresponding to the Mohr failure envelope in the Mohr's diagram (*left*), corresponding nodal lines (in the *middle*) and the P/T axes (*right*). The P/T axes form the P (*red*)/T (*blue*) failure curves displaying the two-wing pattern. The σ_1, σ_2 and σ_3 stress axes have directions (azimuth/plunge): 308°/44°, 209°/9° and 110°/44°. The shape ratio R is 0.5. The azimuth angle is measured clockwise from north (denoted as N), and the plunge angle from the horizontal plane

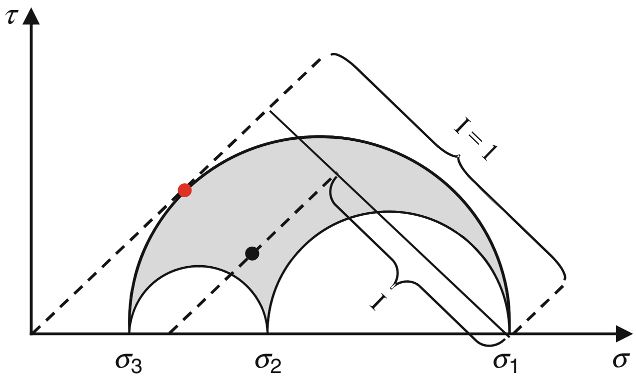

Fig. 8 Definition of the fault instability in the Mohr's diagram. The *red dot* marks the principal fault characterized by instability $I = 1$. The *black dot* marks an arbitrarily oriented fault with instability I. Quantities τ and σ are the shear and the effective normal stresses, respectively; σ_1, σ_2 and σ_3 are the effective principal stresses

where τ_c and σ_c are the shear and effective normal stresses along the principal fault (blue dot in Fig. 6, red dot in Fig. 8), and τ and σ are the shear and effective normal stresses along the analysed fault (black dot in Fig. 8).

Since Eq. 16 is independent of absolute stress values, the fault instability I can be evaluated just from friction μ, shape ratio R,

Encyclopedia of Earthquake Engineering
DOI 10.1007/978-3-642-36197-5_295-1

$$R = \frac{\sigma_1 - \sigma_2}{\sigma_1 - \sigma_3}, \tag{17}$$

and from directional cosines **n** defining the inclination of the fault plane from the principal stress axes (i.e., **n** being expressed in the coordinate system of the principal stress directions). If the reduced stress tensor is scaled as follows:

$$\sigma_1 = 1, \sigma_2 = 1 - 2R, \sigma_3 = -1, \tag{18}$$

where positive values mean compression, stresses τ_c and σ_c along the principal fault read

$$\tau_c = \frac{1}{\sqrt{1+\mu^2}}, \sigma_c = -\frac{\mu}{\sqrt{1+\mu^2}}, \tag{19}$$

and consequently

$$I = \frac{\tau - \mu(\sigma - 1)}{\mu + \sqrt{1+\mu^2}}, \tag{20}$$

where

$$\sigma = n_1^2 + (1-2R)n_2^2 - n_3^2,$$

$$\tau = \sqrt{n_1^2 + (1-2R)^2 n_2^2 + n_3^2 - \left(n_1^2 + (1-2R)n_2^2 - n_3^2\right)^2}. \tag{21}$$

The fault instability can be calculated using Eqs. 20 and 21 for all orientations of fault planes and projected into the focal sphere (see Fig. 9). Such figure is, in particular, helpful when analysing orientations of unstable faults under stress field with inclined principal stress directions.

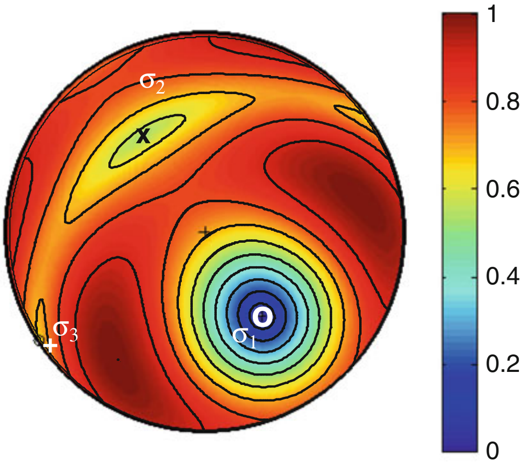

Fig. 9 The fault instability is shown for all possible fault normals; it is colour-scaled and ranges between 0 (the most stable plane) and 1 (the most unstable plane). The lower-hemisphere equal-area projection is used. Directions of the σ_1, σ_2 and σ_3 axes are (azimuth/plunge): 146°/48°, 327°/42° and 237°/1°. The shape ratio R is 0.80 and the fault friction μ is 0.5 (Modified after Vavryčuk et al. (2013))

Encyclopedia of Earthquake Engineering
DOI 10.1007/978-3-642-36197-5_295-1

Principal Focal Mechanisms

As mentioned above, the higher the instability, the higher the probability of the fault being activated. Obviously, a prominent fault plane is the principal fault (Vavryčuk 2011a). This plane is optimally oriented in the stress field and has the highest instability $I = 1$ (see Figs. 6 and 8). Each stress allows for the existence of two distinct principal faults and two distinct principal focal mechanisms (Fig. 10). The reason for the existence of two principal mechanisms is the same as for observing the two-wing pattern of the failure curves and two clusters of focal mechanisms – one principal fault lying in the upper half-plane and the other principal fault in the lower half-plane of the Mohr's circle diagram. The P/T axes of the principal focal mechanisms lie within the two P/T butterfly wings. If the area of unstable faults (see Fig. 6) is decreased, for example, by decreasing pore pressure, the wings become smaller being shrunk to the P/T axes of the principal focal mechanisms in the limit.

The orientation of the principal fault planes and principal focal mechanisms depends on stress and fault friction. The B (neutral) axes of both principal focal mechanisms coincide with the σ_2 axis (Fig. 10b). The P/T axes lie in the σ_1–σ_3 plane: the σ_1 axis is in the centre between the two P axes, and the σ_3 axis is in the centre between the two T axes. The principal fault planes are those nodal planes whose deviation from the σ_1 axis is less than 45°. Deviation θ between the two principal fault planes is expressed by a formula similar to that for the 2-D stress:

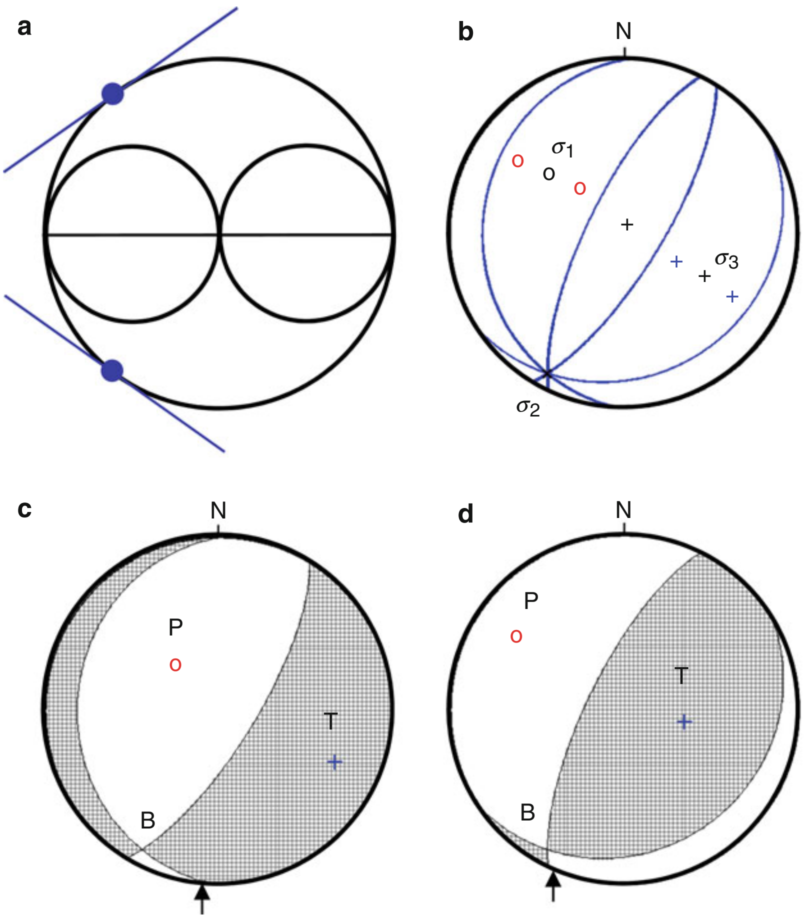

Fig. 10 Principal focal mechanisms. (**a**) Full Mohr's circle diagram, (**b**) principal nodal lines and P/T axes, and (**c**, **d**) principal focal mechanisms. The *blue dot* in (**a**) marks the principal fault plane, the *arrows* in (**c**) and (**d**) denote the nodal lines corresponding to the principal fault plane. Point B in (**c**) and (**d**) denotes the neutral axis, N denotes north (After Vavryčuk (2011a))

$$\mu^{-1} = \tan 2\theta. \tag{22}$$

Since the relation between the principal focal mechanisms and the orientation of stress is simple, the inversion for stress orientation from principal focal mechanisms is straightforward. On the other hand, the shape ratio cannot be retrieved from the principal focal mechanisms. The shape ratio constrains the mutual relation between the size and shape of the P and T butterfly wings. Therefore, a rather large set of focal mechanisms is needed to map the wings accurately. Methods for inversion of stress including the shape ratio from a set of focal mechanisms are described below.

Inversion for Stress From Earthquake Mechanisms

Several methods have been proposed for the determination of stress from a set of focal mechanisms of earthquakes (Maury et al. 2013). These methods usually assume that (1) tectonic stress is uniform (homogeneous) in the region, (2) earthquakes occur on pre-existing faults with varying orientations, (3) the slip vector points in the direction of shear stress on the fault (the so-called Wallace-Bott hypothesis; see, Wallace 1951; Bott 1959), and (4) the earthquakes do not interact with each other and do not disturb the background tectonic stress. Obviously, these conditions might not be always satisfied. Firstly, in case that stress is not uniform, the area should be subdivided into smaller areas in which the condition of uniform tectonic stress is reasonable to assume. Secondly, if a high variety of focal mechanisms is not observed, the inversion yields less accurate results. The smaller variety of the observed focal mechanisms, the larger uncertainty in the stress orientations retrieved. Thirdly, the Wallace-Bott assumption of the slip vector parallel to the stress on the fault is valid only in isotropic media. In anisotropic media, both vectors need not be parallel and the problem becomes more involved, particularly, if anisotropy in the focal zone is not known. Finally, stress changes due to the occurrence of small earthquakes are usually negligible but large earthquakes can significantly affect the background stress field. In this case, inverting for stress should be performed from earthquakes clustered not only in space but also in time and periods between and after a large earthquake should be distinguished.

If the above-mentioned assumptions are reasonably satisfied, the stress inversion methods are capable to determine four parameters of the stress tensor: three angles defining the directions of the principal stress directions, σ_1, σ_2 and σ_3, and shape ratio R. The methods are unable to recover the remaining two parameters of the stress tensor. Therefore, the stress tensor is usually searched with the normalized maximum compressive stress

$$\sigma_1 = +1, \tag{23}$$

and with the zero trace

$$Tr(\boldsymbol{\tau}) = \sigma_1 + \sigma_2 + \sigma_3 = 0. \tag{24}$$

This implies that no information about pore pressure, which is isotropic, can be gained from the focal mechanisms.

Next, the individual approaches to stress inversion are described and their pros and cons are mentioned.

Michael Method

A simplest approach to stress inversion is the method of Michael (1984). This method employs Eq. 4 expressed in the following form:

$$\tau_{kj}n_j(\delta_{ik} - n_i n_k) = \tau N_i. \tag{25}$$

In order to be able to evaluate the right-hand side of the equation, Michael (1984) applies the Wallace-Bott assumption that direction **N** of shear stress component of traction **T** on a fault is identical with the slip direction **s**, and he further assumes that shear stress τ on activated faults has the same value for all studied earthquakes. Since the method cannot determine absolute stress values, τ in Eq. 25 is assumed to be 1 and Eq. 23 is not applied. Subsequently, Eq. 25 is expressed in the matrix form

$$\mathbf{At} = \mathbf{s}, \tag{26}$$

where **t** is the vector of stress components

$$\mathbf{t} = [\tau_{11} \quad \tau_{12} \quad \tau_{13} \quad \tau_{22} \quad \tau_{23}], \tag{27}$$

A is the 3 × 5 matrix calculated from fault normal **n**,

$$\begin{bmatrix} n_1(n_2^2 + 2n_3^2) & n_2(1 - 2n_1^2) & n_3(1 - 2n_1^2) & n_1(-n_2^2 + n_3^2) & -2n_1n_2n_3 \\ n_2(-n_1^2 + n_3^2) & n_1(1 - 2n_2^2) & -2n_1n_2n_3 & n_2(n_1^2 + 2n_3^2) & n_3(1 - 2n_2^2) \\ n_3(-2n_1^2 - n_2^2) & -2n_1n_2n_3 & n_1(1 - 2n_3^2) & n_3(-n_1^2 - 2n_2^2) & n_2(1 - 2n_3^2) \end{bmatrix}, \tag{28}$$

and **s** is the unit direction of the slip vector. Extending Eq. 28 for focal mechanisms of K earthquakes with known fault normals **n** and slip directions **s**, a system of 3 × K linear equations for five unknown components of stress tensor is obtained. The system is solved using the generalized linear inversion in the L2-norm (Lay and Wallace 1995, their Section 6.4)

$$\mathbf{t} = \mathbf{A}^{-g}\mathbf{s}. \tag{29}$$

The basic drawback of this method is the necessity to know orientations of the faults. Usually, when determining the focal mechanisms, orientations of the two nodal planes are calculated: one nodal plane corresponding to the fault and the other nodal plane (called the auxiliary plane) defining the slip direction. The inherent ambiguity of focal mechanisms does not allow distinguishing easily which of the nodal planes is the fault. If the Michael's method is used with incorrect orientations of the fault planes, the accuracy of the retrieved stress tensor is decreased. On the other hand, the method is quite fast and it can be run repeatedly. Therefore, the confidence regions of the solution are determined using the standard bootstrap method (Michael 1987). If the orientation of fault planes in the focal mechanisms is unknown, each nodal plane has a 50 % probability of being chosen during the bootstrap resampling.

Recently, Vavryčuk (2014) modified the Michael's method and removed the difficulty with the unknown fault orientations. He proposed inverting jointly for stress and for the fault orientations by applying the fault instability constraint. According to this constraint, the fault is identified with that nodal plane which has a higher value of instability calculated using Eq. 20. The stress is calculated in iterations and overall friction μ on faults is also determined. Numerical tests show that the iterative stress inversion is fast and accurate and performs better than the standard Michael's inversion.

Angelier Method

The difficulty with determining the fault plane in the focal mechanisms is also overcome in the method developed by Angelier (2002). This method is based on maximizing the slip shear stress component (SSSC) along the fault

DOI 10.1007/978-3-642-36197-5_295-1

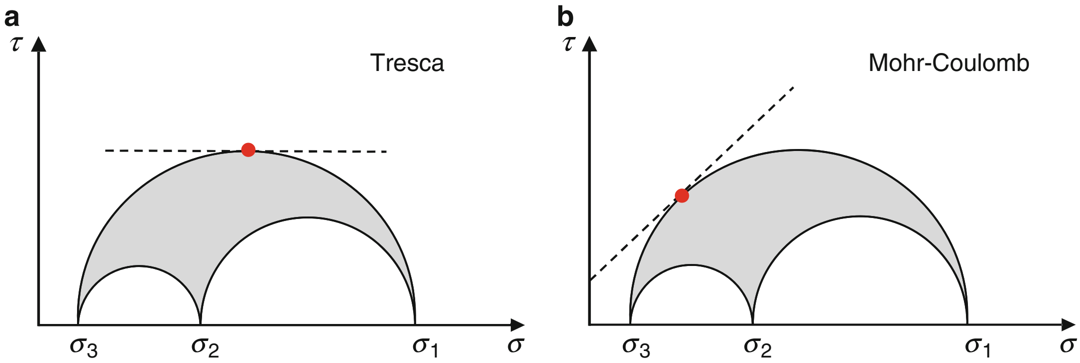

Fig. 11 Tresca and Mohr-Coulomb failure criteria. The Tresca failure criterion is unphysical and corresponds to a fault with zero friction. The *red dot* marks the principal fault plane

$$\tau_s = T_i s_i = \tau_{ij} n_i s_j. \tag{30}$$

Since the SSSC value is symmetric with respect to vectors **n** and **s**, it is invariant of the choice of the fault plane from the two nodal planes. The condition of the maximum shear stress Eq. 30 is not fully correct and physically means that faults should obey the so-called Tresca failure criterion where faults are assumed to have zero friction. Only faults with zero friction can achieve maximum shear stress and satisfy Eq. 30; for faults with friction, the SSSC value is always reduced (see Fig. 11).

For K focal mechanisms, the total SSSC value is maximized as follows:

$$\tau_s^{\text{total}} = \frac{\tau_{ij}}{\tau_{\max}} \sum_{k=1}^{K} n_i^{(k)} s_j^{(k)}, \tag{31}$$

where

$$\tau_{\max} = \frac{\sigma_1 - \sigma_3}{2}. \tag{32}$$

and the optimum stress tensor is calculated analytically (see Angelier 2002). An alternative approach defines the total SSSC value in the form:

$$\tau_s^{\text{total}} = \tau_{ij} \sum_{k=1}^{K} n_i^{(k)} s_j^{(k)}, \tag{33}$$

with the normalization condition

$$\sigma_1^2 + \sigma_2^2 + \sigma_3^2 = 1. \tag{34}$$

and with the zero trace condition Eq. 24. In this case, the inversion for the optimum stress tensor can be performed using a grid search through the principal stress directions and shape ratio R. The fit function is maximized in the L1-norm.

Although the condition of maximizing the SSSC value looks as a rather rough approximation, its use in practice is advocated by Angelier (2002) for the following reasons. Firstly, the activated fault planes are located mostly close to the top of the Mohr's circle diagram. For example, friction of 0.6 reduces the

DOI 10.1007/978-3-642-36197-5_295-1

maximum shear stress by 13 % only. Secondly, numerical tests show that if focal mechanisms inverted display a sufficient variety, maximizing the SSSC value leads to a small bias in the retrieved stress directions. Thirdly, maximizing the SSSC value is quite robust with respect to the errors present in focal mechanisms.

Gephart and Forsyth Method

Another way how to solve the problem with ambiguous fault plane orientations in stress inversions is proposed by Gephart and Forsyth (1984). The method is based on minimizing the deviation between direction **N** of shear stress and slip direction **s** along the fault. This deviation is calculated for both options of the fault orientation and the lower value enters into the total sum over all K focal mechanisms minimized during the inversion:

$$S = \sum_{k=1}^{K} \operatorname{acos}\left(\mathbf{N}^{(k)} \cdot \mathbf{s}^{(k)}\right). \tag{35}$$

The method was further modified and improved by Lund and Slunga (1999) who applied a more physical criterion for identifying the true fault planes. The criterion is based on the evaluation of instability of the fault using Eq. 20 and the fault plane is identified with that nodal plane which is more unstable and thus more susceptible to failure under the given stress field. The misfit function is minimized in the L1-norm by using the robust grid search inversion scheme. It is also possible to exclude a predefined number of outliers from the misfit function the result of the inversion to be less sensitive to large errors in input data. Since the misfit function is usually smooth and simple, the time-consuming grid search can be substituted by any non-linear inversion method. For example, the gradient or simplex methods can be applied with a success. This applies also to the Angelier method defined by Eqs. 33 and 34.

Accuracy of Stress Inversion Algorithms: Numerical Tests

The robustness and accuracy of the stress inversion methods can be efficiently tested using numerical modelling. The key parameters of any stress inversion are the number of focal mechanisms inverted, their accuracy and variability. The inversions yield orientations of the principal stress axes and shape ratio R.

Numerical tests performed with sets of 25–250 focal mechanisms are presented. The stress tensor is fixed for all datasets. The focal mechanisms are selected to satisfy the Mohr-Coulomb failure criterion (see Fig. 12a,b) and subsequently they are used for the calculation of moment tensors. The moment tensors were contaminated by uniform noise ranging from 0 to ±50 % of the norm of the moment tensor (calculated as the maximum of absolute values of the moment tensor eigenvalues). The noisy moment tensors were decomposed back into strikes, dips and rakes of noisy focal mechanisms inverted for stress. The deviation between the true and noisy fault normals and slips attained values from 0° to 25° (see Fig. 13). Since the inverted focal mechanisms were calculated from moment tensors, knowledge of the orientation of the fault planes was lost in the data set. The inversion was run repeatedly using 50 realizations of random noise and for two types of sets of focal mechanisms. The first set consisted of focal mechanisms which projected into both half-planes of the Mohr's circle diagram and thus covered both butterfly wings in the P/T plot (see Fig. 12, left plots). The second set consisted of focal mechanisms projected just into upper half-plane of the Mohr's circle diagram and covered just one butterfly wing in the P/T plot (see Fig. 12, right plots). The inverted principal stress directions and shape ratios for both data

Encyclopedia of Earthquake Engineering
DOI 10.1007/978-3-642-36197-5_295-1

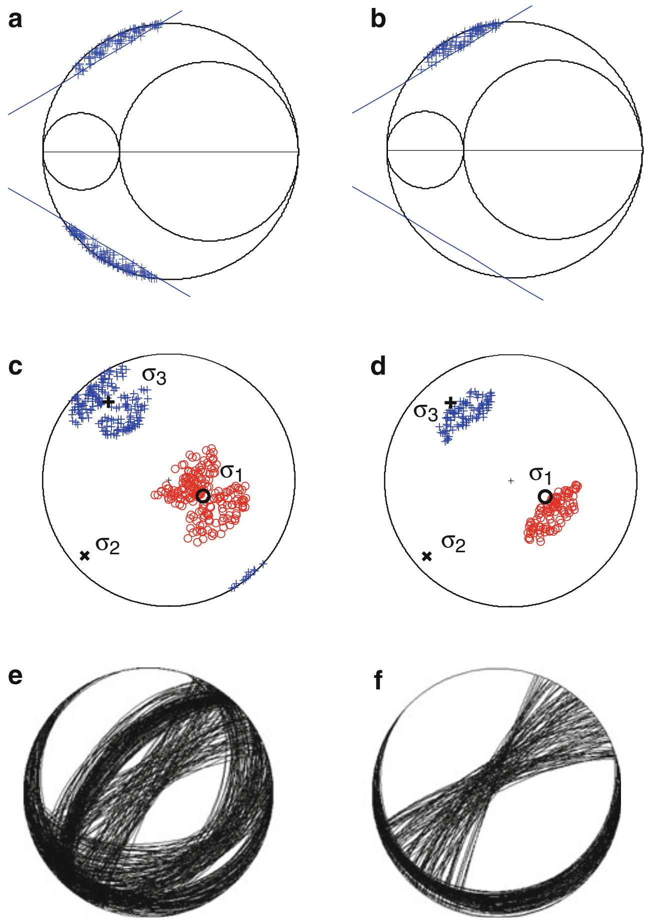

Fig. 12 Example of data used in numerical tests of stress inversions. The plots show 200 noise-free focal mechanisms selected to satisfy the Mohr-Coulomb failure criterion. *Left*/*right* plots – dataset with a full/reduced variety of focal mechanisms. (**a**, **b**) Mohr's circle diagrams, (**c**, **d**) P/T axes and (**e**, **f**) corresponding nodal lines. The P axes are marked by the *red circles* and T axes by the *blue crosses* in (**c**) and (**d**). The σ_1, σ_2 and σ_3 stress axes are (azimuth/plunge): 115°/65°, 228°/10° and 322°/23°, respectively. Shape ratio R is 0.70, cohesion C is 0.85, pore pressure p is zero and friction μ is 0.60. The minimum instability of faults is 0.82

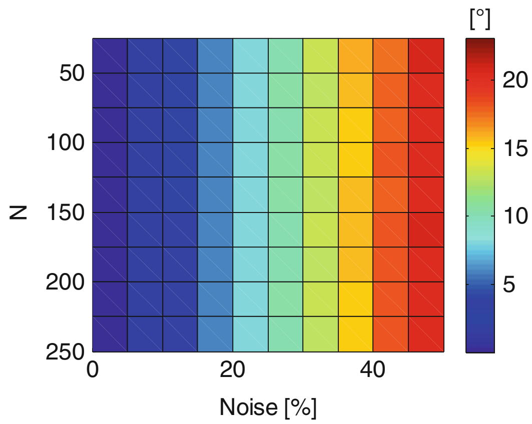

Fig. 13 Mean deviation of noisy fault normals as a function of noise superimposed on the moment tensors. The deviation is colour-coded and evaluated in degrees. The noisy slip directions display the same deviations

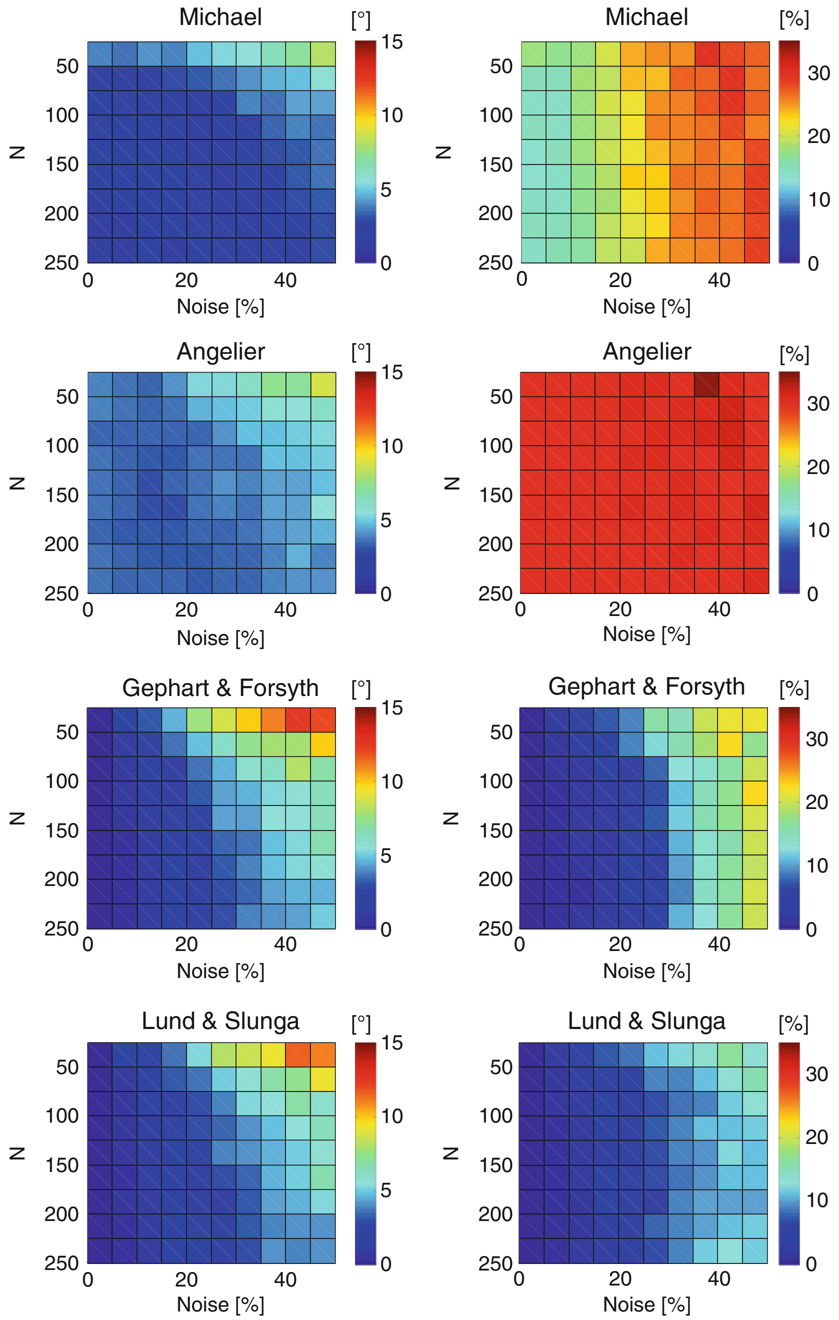

Fig. 14 Mean error of principal stress directions (*left*) and of the shape ratio (*right*) as a function of the number of inverted focal mechanisms and noise in moment tensors. The data set with the full variety of focal mechanisms (two-wings data) is inverted. The errors are shown for the method of Michael (1984), Angelier (2002), Gephart and Forsyth (1984) and Lund and Slunga (1999). The method of Angelier (2002) employs Eqs. 33 and 34. The errors are calculated from 50 random realizations of noise. The errors in the stress directions are in degrees, the errors in the shape ratio are in percent

sets and all realizations of random noise were compared with the true values and the errors were evaluated (see Figs. 14 and 15).

The tests indicate that the accuracy of the stress inversions significantly varies and strongly depends on noise in the data and on the number of focal mechanisms inverted. All inversions yield satisfactory results for the principal stress directions with an average error less than 15° for 25 noisy focal mechanisms

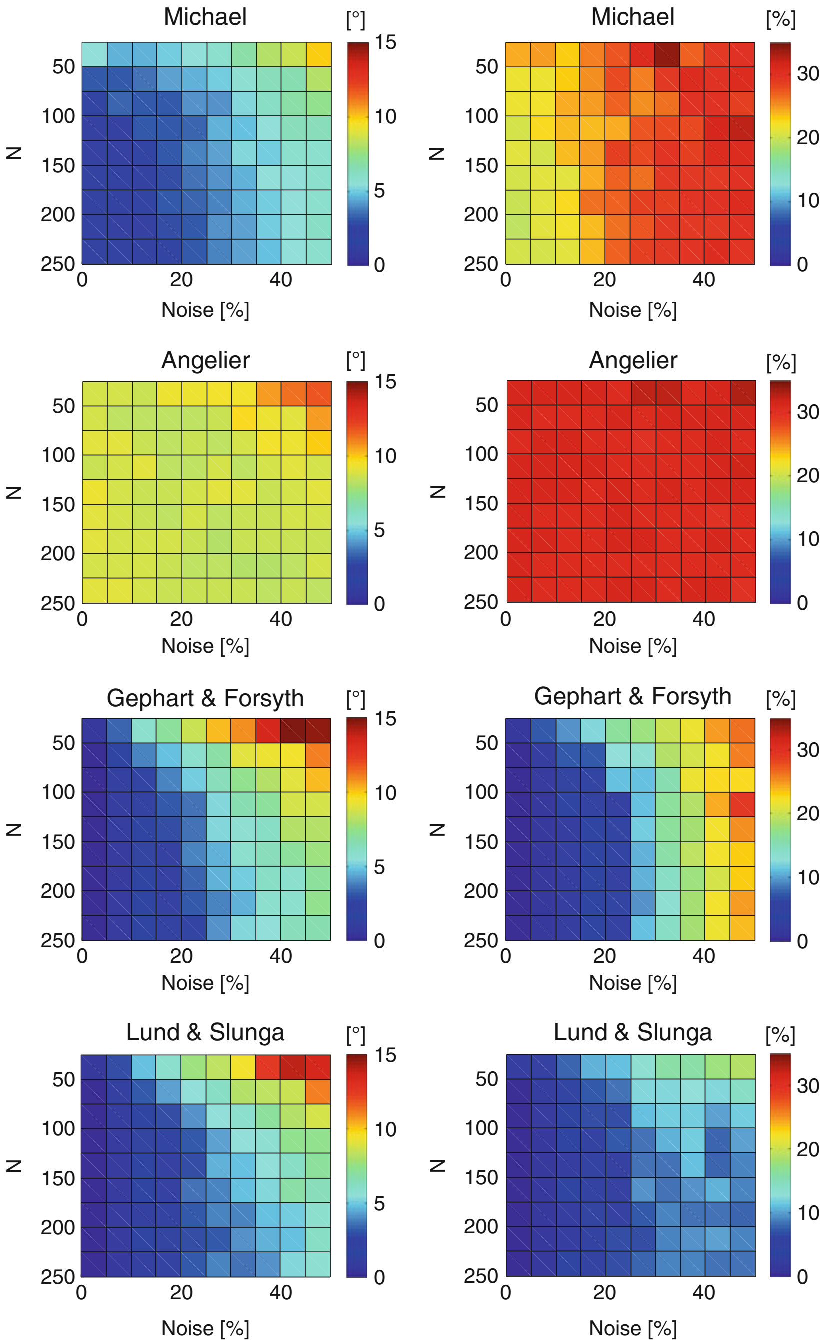

Fig. 15 The same as for Fig. 14, but for the data set with the reduced variety of focal mechanisms (one-wing data)

inverted (see Fig. 14, left plots). If a reduced variety of focal mechanisms was used (see Fig. 15, left plots), the method of Angelier (2002) produced systematically worse results than the other methods. The errors occurred even in the case of 250 noise-free focal mechanisms. Slightly biased results for noise-free data were produced also by the method of Michael (1984), because this method is sensitive to the ambiguity in the orientation of fault planes.

In addition, the tests reveal that the shape ratio is a more critical parameter than the orientation of the principal stress directions (see Figs. 14 and 15, right plots). The method of Angelier (2002) completely failed even when the high number of noise-free focal mechanisms of the full variety were inverted (see

Encyclopedia of Earthquake Engineering
DOI 10.1007/978-3-642-36197-5_295-1

Fig. 14) yielding the shape ratio of about 0.5 instead of 0.7. Also the method of Michael (1984) works significantly worse than the method of Gephart and Forsyth (1984) and its modification proposed by Lund and Slunga (1999). The latter two methods produce results of similar accuracy, the method of Lund and Slunga (1999) working slightly better and being less sensitive to the low number of focal mechanisms, high noise in the data and the limited variability of focal mechanisms (see Fig. 15, right plots).

Inversion for Temporal or Spatial Variation of Stress

With an increasing number and accuracy of focal mechanisms of earthquakes occurring in seismically active regions, it becomes possible to study spatial variations of stress or its temporal evolution. The simplest approach how to study the spatial variation of stress is to subdivide the study area into subareas or cells of a similar stress regime and invert for stress of individual cells. Similarly, in case of the time evolution of stress, the total time period of observations can be split into several phases of the seismic activity and stress can be inverted for individual time windows. In order to increase the number of focal mechanisms inverted, the individual cells or time windows can partly overlap. This produces smooth results highlighting their large-scale lateral variations or long-period trends being very analogous to the moving average method.

The mentioned stress inversions can be exemplified on several applications. The simplest approach, when the area under study is subdivided just into two subareas of different stress regimes, was presented, for example, by Vavryčuk (2006) for deep earthquakes in the Tonga subducting slab (see Fig. 16). The slab is considerably deformed at depths between 500 and 670 km and can be subdivided into two

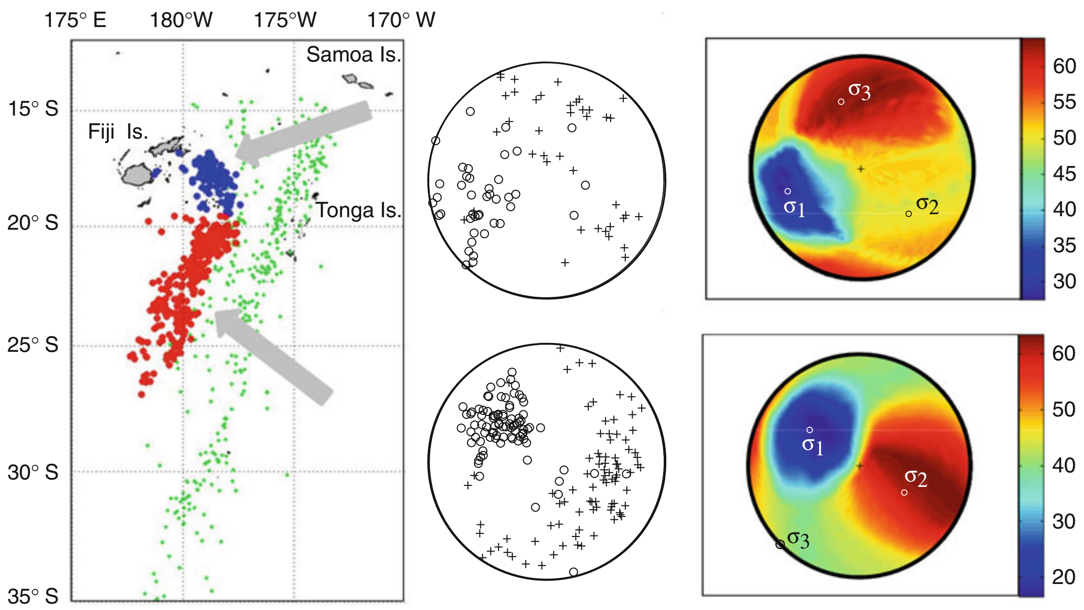

Fig. 16 Inversion for stress in the Tonga subduction zone. *Left plot* – the map view with epicentres of earthquakes. *Green dots* mark earthquake foci at depths between 100 and 500 km, *blue*/*red* dots mark deep-focus earthquakes at depths greater than 500 km in the northern/southern cluster. The *grey arrows* show the horizontal projections of the maximum compression in the northern/southern cluster. *Middle plots* – P axes (*circles*) and T axes (*plus signs*) of focal mechanisms distributed over the focal sphere for earthquakes from the northern (*upper plot*) and southern (*lower plot*) slab segments. *Right plots* – the misfit function for the principal stress axis σ_1, defined as the average deviation (in degrees) between the predicted shear stress directions and the observed slips at the faults. The Gephart and Forsyth inversion method (1984) was applied. The optimum directions of the principal stresses are marked by *circles* (Modified after Vavryčuk (2006))

DOI 10.1007/978-3-642-36197-5_295-1

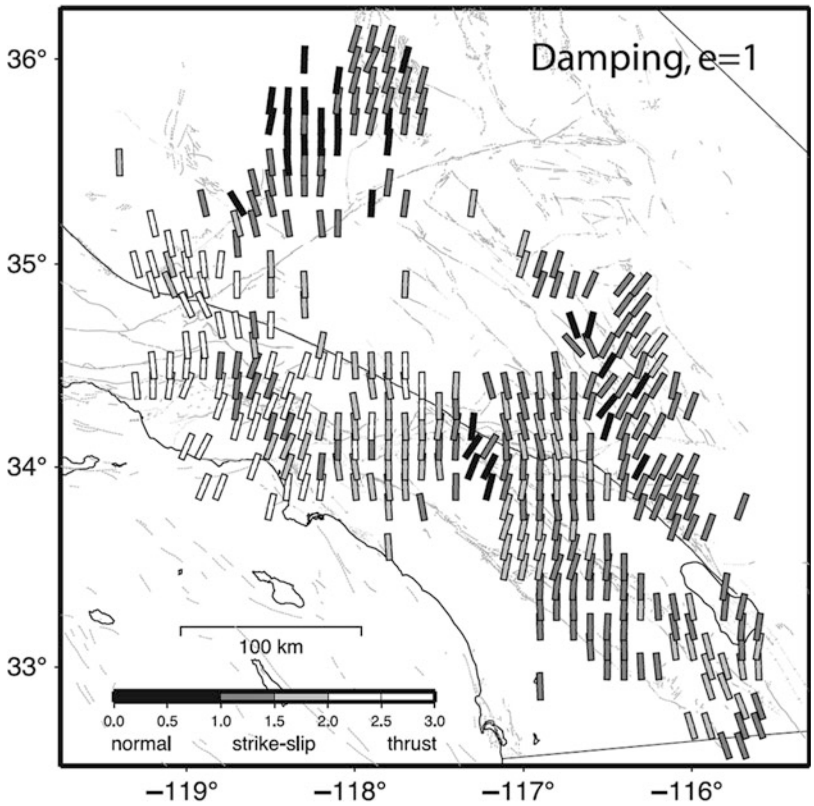

Fig. 17 Stress inversion for southern California. A data set of 6957 focal mechanisms is inverted for the stress tensor at points on a 0.1° grid. The bar orientation shows the direction of the maximum horizontal stress axis, and the shading of the bar indicates the stress regime, following Simpson (1997). *Light grey lines* show mapped fault traces, and the *black line* shows the San Andreas Fault. The damped inversion method of Hardebeck and Michael (2006) is used with damping parameter e = 1 (After Hardebeck and Michael (2006), their figure 5c)

segments of different orientations characterized by different principal stress directions. The stress inversion shows that the maximum compressive stress is directed along the down-dip motion of the slab in both segments. A more detailed mapping of lateral variations of stress obtained from focal mechanisms was published by Hardebeck (2006) for Southern California who employed the stress inversion code SATSI developed by Hardebeck and Michael (2006). This code inverts simultaneously for stress in all subareas of the region under study and minimizes the difference in stress between adjacent subareas to suppress over fitting of noisy data (see Fig. 17). A modification of this code, called MSATSI and working in the Matlab environment, was applied by Ickrath et al. (2014) to analyse spatial and temporal variations of stress prior and after the 1999 Mw 7.4 Izmit earthquake in Turkey. This analysis revealed systematic rotations of stress related to the occurrence of the Izmit earthquake. The rotation of the principal stress directions have been observed also after the 1999 Mw 7.6 Chi-Chi earthquake in Taiwan (Wu et al. 2010) and for the 2011 Mw 9 Tohoku-oki earthquake in Japan (Yang et al. 2013). Spatial and temporal variations of stress from focal mechanisms have been studied also for New Zealand (Townend et al. 2012) with focus on the 2010 Mw 6.2 Christchurch earthquake, and for other seismoactive regions including geothermal fields in which seismicity is induced by fluid injections (Martínez-Garzón et al. 2013).

DOI 10.1007/978-3-642-36197-5_295-1

Summary

The stress field and fracture processes in the Earth's crust are closely related phenomena. Fracturing is controlled by shear stress on the fault, pore-fluid pressure, cohesion and fault friction. In addition, the orientation of the fault with respect to the principal stress directions governs susceptibility of the fault to be ruptured. An essential role in the stress analysis play principal faults – the faults which are optimally oriented for shear faulting and thus being the most unstable under the given stress conditions. The type of faulting, the orientation of the activated faults and the direction of the slip along the faults can be inverted for stress and its spatial and temporal variations within the Earth's crust. The stress inversions work best if the fault orientations are known. If the fault plane cannot be uniquely identified from the focal mechanisms, the inversions are less accurate. The inversions are capable to retrieve four stress parameters: the principal stress directions and the shape ratio. The accuracy of the results depends on the applied inversion method, on the number of inverted focal mechanisms, their errors and variety. The most critical parameter is the shape ratio, which can be successfully recovered only by the Gephart and Forsyth (1984), Lund and Slunga (1999) and Vavryčuk (2014) methods provided that a high number of accurate focal mechanisms is available.

Cross-References

► Earthquake Mechanism Description and Inversion
► Earthquake Mechanisms and Tectonics
► Non-Double-Couple Earthquakes

References

Anderson EM (1951) The dynamics of faulting. Oliver & Boyd, Edinburgh

Angelier J (2002) Inversion of earthquake focal mechanisms to obtain the seismotectonic stress IV – a new method free of choice among nodal lines. Geophys J Int 150:588–609

Bott MHP (1959) The mechanics of oblique slip faulting. Geol Mag 96:109–117

Byerlee J (1978) Fiction of rocks. Pure Appl Geophys 116:615–626

Fischer T, Guest A (2011) Shear and tensile earthquakes caused by fluid injection. Geophys Res Lett 38, L05307. doi:10.1029/2010GL045447

Fowler CMR (1990) The solid earth. An introduction to global geophysics. Cambridge University Press, Cambridge

Gephart JW, Forsyth DW (1984) An improved method for determining the regional stress tensor using earthquake focal mechanism data: application to the San Fernando earthquake sequence. J Geophys Res 89:9305–9320

Hardebeck JL (2006) Homogeneity of small-scale earthquakes faulting, stress, and fault strength. Bull Seismol Soc Am 96:1675–1688

Hardebeck JL, Michael AJ (2006) Damped regional-scale stress inversions: methodology and examples for southern California and the Coalinga aftershock sequence. J Geophys Res 111, B11310

Heidbach O, Tingay M, Barth A, Reinecker J, Kurfeß D, Müller B (2008) The world stress map database release 2008. doi:10.1594/GFZ.WSM.Rel2008

Ickrath M, Bohnhoff M, Bulut F, Dresen G (2014) Stress rotation and recovery in conjunction with the 1999 Izmit Mw 7.4 earthquake. Geophys J Int 196:951–956

Jaeger JC, Cook NGW, Zimmerman RW (2007) Fundamentals of rock mechanics, 4th edn. Blackwell, Oxford

Julian BR, Miller AD, Foulger GR (1998) Non-double-couple earthquakes. 1. Theory. Rev Geophys 36:525–549

Lay T, Wallace TC (1995) Modern global seismology. Academic, New York

Lund B, Slunga R (1999) Stress tensor inversion using detailed microearthquake information and stability constraints: application to Ölfus in southwest Iceland. J Geophys Res 104:14947–14964

Martínez-Garzón P, Bohnhoff M, Kwiatek G, Dresen G (2013) Stress tensor changes related to fluid injection at The Geysers geothermal field, California. Geophys Res Lett 40:2596–2601

Maury J, Cornet FH, Dorbath L (2013) A review of methods for determining stress fields from earthquake focal mechanisms: application to the Sierentz 1980 seismic crisis (Upper Rhine graben). Bull Soc Geol Fr 184(4–5):319–334

Mavko G, Mukerji T, Dvorkin J (2009) The rock physics handbook. Tools for seismic analysis in porous media. 2nd edition. Cambridge University Press, Cambridge

Michael AJ (1984) Determination of stress from slip data: faults and folds. J Geophys Res 89:11517–11526

Michael AJ (1987) Use of focal mechanisms to determine stress: a control study. J Geophys Res 92(B1):357–368

Ruff LJ (2002) State of stress within the earth. In: Lee WHK, Kanamori H, Jennings PC, Kisslinger C (eds) International handbook of earthquake and engineering seismology. Part A. Academic, New York

Scholz CH (2002) The mechanics of earthquakes and faulting. Cambridge University Press, Cambridge

Simpson RW (1997) Quantifying Anderson's fault types. J Geophys Res 102:17909–17919

Townend J, Sherburn S, Arnold R, Boese C, Woods L (2012) Three-dimensional variations in present-day tectonic stress along the Australia–Pacific plate boundary in New Zealand. Earth Planet Sci Lett 353–354:47–59

Vavryčuk V (2006) Spatially dependent seismic anisotropy in the Tonga subduction zone: a possible contributor to the complexity of deep earthquakes. Phys Earth Planet Inter 155:63–72. doi:10.1016/j.pepi.2005.10.005

Vavryčuk V (2011a) Principal earthquakes: theory and observations from the 2008 West Bohemia swarm. Earth Planet Sci Lett 305:290–296. doi:10.1016/j.epsl.2011.03.002

Vavryčuk V (2011b) Tensile earthquakes: theory, modeling, and inversion. J Geophys Res 116, B12320. doi:10.1029/2011JB008770

Vavryčuk V (2014) Iterative joint inversion for stress and fault orientations from focal mechanisms. Geophys J Int 199(1):69–77. doi:10.1093/gji/ggu224

Vavryčuk V, Bouchaala F, Fischer T (2013) High-resolution fault image from accurate locations and focal mechanisms of the 2008 swarm earthquakes in West Bohemia, Czech Republic. Tectonophysics 590:189–195. doi:10.1016/j.tecto.2013.01.025

Wallace RE (1951) Geometry of shearing stress and relation to faulting. J Geol 59:118–130. doi:10.1086/625831

Wu Y-M, Hsu Y-J, Chang C-H, Teng LS, Nakamura M (2010) Temporal and spatial variation of stress field in Taiwan from 1991 to 2007: insights from comprehensive first motion focal mechanism catalog. Earth Planet Sci Lett 298:306–3016

Yang,Y-R, Johnson, KM, Chuang, RY (2013) Inversion for deviatoric absolute crustal stress using focal mechanisms and coseismic stress changes: The 2001 M9 Tohoku-oki, Japan, earthquake, J Geophys Res 118:5516–5529

Zang A, Stephansson O (2010) Stress field of the earth's crust. Springer, New York

Zoback MD (2007) Reservoir geomechanics. Cambridge University Press, Cambridge